DNS of Laminar-Turbulent Transition in Separation Bubbles

U. Maucher, U. Rist, M. Kloker, and S. Wagner

Institut für Aerodynamik und Gasdynamik, Universität Stuttgart,
Pfaffenwaldring 21, 70550 Stuttgart, Germany

Abstract. A Laminar Separation Bubble (LSB) is created under the influence of an adverse (positive) pressure gradient along a wall by laminar separation, laminar-turbulent transition and turbulent re-attachment of the flow to the wall. Direct Numerical Simulations (DNS) of the flow in an airfoil boundary layer which are based on solving the full Navier–Stokes equations exhibit good quantitative agreement of the mean-flow data with wind-tunnel experiments, but only examinations of the unsteady results are able to reveal the underlying physics. Thus, a hitherto unknown temporal amplification of three-dimensional small-amplitude disturbances is observed and explained by the entrainment of three-dimensional fluctuations by the roll-up of the detached boundary layer. Once the three-dimensional disturbances become saturated this mechanism leads to a rapid breakdown of the laminar flow into regions of small-scale turbulence which are organized in a quasi two-dimensional coherent manner.

1 Introduction

When an object is placed in a fluid flow, a boundary layer develops close to its surface. Drag is caused by the friction due to fluid viscosity in the boundary layer and lift is influenced by the thickness of the boundary layer. For small disturbance environments, such as flight in the atmosphere, a laminar boundary layer develops starting from the stagnation region. But further downstream it becomes turbulent by what is called laminar-turbulent transition. The present work is part of ongoing research on laminar-turbulent transition using the Direct Numerical Simulation (DNS) technique (solution of the complete Navier–Stokes equations) in the HLRS-project LAMTUR. Results for transition behind a periodically forced point source on a wing have already been presented in [8]. In the present paper the focus will be on transition in a so-called Laminar Separation Bubble (LSB) on an airfoil section of a glider plane.

Figure 1 shows a typical wing section together with its surface pressure distribution for a certain angle of attack and Reynolds number where LSBs on the upper and lower surface of the airfoil lead to characteristic pressure plateaus (pointed out by circles). In these regions the boundary layer separates and undergoes transition. Because of the enhanced transversal momentum exchange caused by turbulence the flow is able to re-attach as a turbulent

boundary layer at the position where the pressure increases (note the direction of the pressure coefficient c_p in Fig. 1). A snapshot of the instantaneous flow in the vicinity of a LSB is shown in Fig. 2. The dark line emanating from the lower left corner is the separating shear layer which starts to oscillate and to roll up into discrete vortices in the right part of the figure. Apparently, transition is connected to the instability of the shear layer.

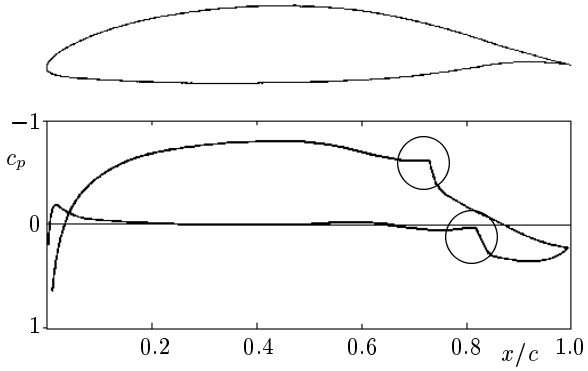

Fig. 1. Airfoil at $Re = 700{,}000$ and $\alpha = -0.5^o$ angle of attack showing the influence of laminar separation bubbles on the surface pressure (circles).

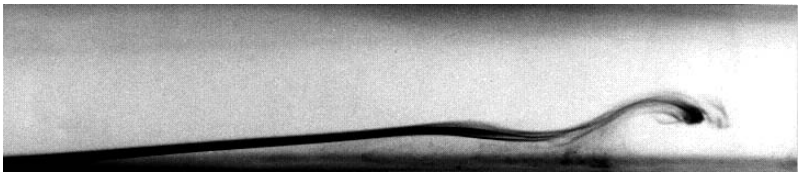

Fig. 2. Experimental flow visualization of the detached boundary layer in a laminar separation bubble.

In practice, LSBs are difficult to predict from wind tunnel data as well as by means of computations. We attribute this to a lack of knowledge and understanding of the underlying physics which are closely related to laminar-turbulent transition of the separated boundary layer. Thus, prior to the beginning of the present research in 1993 no three-dimensional (3D) simulations have been performed for flows with LSBs simply because of the lack of large and fast enough computers. It was known that the separated boundary layer develops into a kind of free shear layer which is highly unstable with respect to two-dimensional (2D) disturbance waves (cf. Fig. 2) and it was speculated that a sequence of secondary and higher-order instabilities with respect to 3D disturbances will lead to the inherently three-dimensional

turbulence. Whether this is true and whether the reverse-flow region underneath the detached shear layer has a non-negligible influence which might lead to a temporal disturbance growth, a so-called absolute instability, was completely unknown. Wind-tunnel experiments intended to answer such questions are extremely difficult to perform because of the high sensitivity of the flow with respect to disturbances caused by the tunnel and the measuring devices. To date, there are almost no experimental data available which describe the instantaneous 3D flow field. Theoretical investigations need to solve the complete Navier–Stokes equations in order to obtain a reliable base flow for investigations based on linear stability theory (LST).

The present project which relies on DNS and careful stability calculations using LST has already made several contributions to a better understanding of instability and transition in LSBs. In [6] and [7] it was shown that LST can be reliably applied for two- and three-dimensional disturbances if the base flow profiles computed in DNS are analyzed. The supposed secondary instability plays a less important role than originally assumed because of two reasons: The secondary disturbance amplification rates are barely higher than the very large primary amplification rates (according to LST) and an unexpected reduction of the 3D growth rate occurs after saturation of the 2D disturbance. Yet, the nonlinear interaction of weakly-oblique traveling waves was found to be the fastest route to turbulence in these earlier investigations. At the same time this mechanism produces longitudinal vortices in the reattachment zone which have also been detected in some earlier experiments.

When the Reynolds number based on the displacement thickness at laminar separation was increased from approximately $Re_{\delta_{1,s}} = 1250$ to $Re_{\delta_1,s} = 2500$, a new mechanism of secondary instability was observed: In the presence of a large-amplitude 2D-wave, 3D-modes are temporally amplified. This mechanism has been firstly reported by Maucher *et al.* [4]. The investigations presented here focus on this mechanism and its impact on the transition in a LSB.

2 Numerical Method

The numerical method was developed in the research-group "Transition and Turbulence" of the *Institut für Aerodynamik und Gasdynamik, IAG*. It is based on the complete Navier–Stokes equations in vorticity-velocity formulation for an incompressible fluid. All variables are non-dimensionalized by a reference length $\hat{L}$, by the velocity $\hat{U}_\infty$, and the variables in wall-normal direction y and v are stretched with the square-root of the Reynolds number $Re = \hat{U}_\infty \hat{L}/\hat{\nu}$, where $\hat{}$ denotes dimensional variables and $\hat{\nu}$ is the kinematic viscosity

$$x = \hat{x}/\hat{L};\ y = \sqrt{Re}\,\hat{y}/\hat{L};\ z = \hat{z}/\hat{L};\ u = \hat{u}/\hat{U}_\infty;\ v = \sqrt{Re}\,\hat{v}/\hat{U}_\infty;\ w = \hat{w}/\hat{U}_\infty. \tag{1}$$

This leads to the definition of the non-dimensionalized vorticity components

$$\omega_x = \frac{1}{Re}\frac{\partial v}{\partial z} - \frac{\partial w}{\partial y}, \quad \omega_y = -\frac{\partial u}{\partial z} + \frac{\partial w}{\partial x}, \quad \omega_z = \frac{\partial u}{\partial y} - \frac{1}{Re}\frac{\partial v}{\partial x}. \tag{2}$$

A flat-plate boundary-layer is subjected to an adverse pressure gradient by prescribing the edge velocity distribution u_e at the upper boundary of a rectangular integration domain (Fig. 3). Basically, u_e may be an arbitrary function of the streamwise coordinate x but here it is taken from experimental measurements. A refined, very accurate boundary-layer interaction model (Maucher *et al.* [5]) captures the displacement effect (index ν) of the boundary layer (in particular of the LSB) and models its influence on the initially prescribed potential velocity distribution u_p yielding an instantaneous edge-velocity distribution:

$$u_e(x,t) = u_p(x) + u_\nu(x,t). \tag{3}$$

From the experiments, two boundary-layer edge-velocity distributions are available (Fig. 3b). The first one (squares) refers to a flow with separation bubble and for the second, turbulent one (triangles), separation has been suppressed by fixing a turbulator upstream of the separation bubble. For the computations, the turbulent distribution has been prescribed as initial condition u_p at the free-stream boundary. Maucher *et al.* [5] show that the displacement effects are captured correctly by their new viscous-inviscid interaction model, and finally the edge velocity distribution u_e comes very close to the experimental measurements with separation bubble.

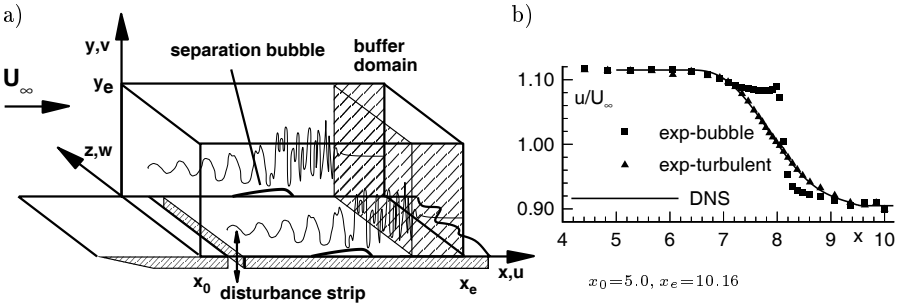

Fig. 3. Integration Domain (a) and comparison of edge-velocity distribution between experiment and DNS (b).

Steady flow is assumed at the inflow boundary and in a disturbance strip at the wall, artificial 2-D and 3-D disturbances can be excited by periodic or pulse-wise, wall-normal suction and blowing. Upstream of the outflow boundary a buffer domain is applied, which damps the unsteady component of the flow smoothly to zero [3].

2.1 Numerical and Computational Aspects

In order to reduce the computational effort, the flow field is assumed to be periodic in spanwise direction z and symmetric initial and boundary conditions are exploited by calculating a symmetric flow field with respect to z=0. A Fourier spectral ansatz with a number of $(2K+1)$ modes is used to transform the variables and equations into Fourier space and vice versa:

$$f(x,y,z,t) = \sum_{k=-K}^{K} F_k(x,y,t) e^{ik\gamma_0 z}\,, \tag{4}$$

where f, and F_k designate the variables in physical, and in spectral space, respectively. The basic spanwise wave number γ_0 for the fundamental Fourier mode (k=1) is related to the spanwise width λ_z of the integration domain through $\gamma_0 = 2\pi/\lambda_z$. The remaining spatial dimensions are discretized by fourth-order accurate finite differences which are employed in alternating upwind/downwind manner for the streamwise convective terms in order to increase numerical stability for long-time integration where time integration is based on a fourth-order Runge-Kutta scheme (cf., Kloker [2]). Thus, the spanwise Fourier ansatz principally reduces the 3-D problem in physical space to a set of (K+1) 2-D problems in Fourier space enabling a largely parallel computation in Fourier space. However, the modes are coupled by the nonlinear convective terms of the vorticity transport equations and are transformed to physical space for the calculation of the nonlinear vorticity terms ("pseudo-spectral method" with de-aliasing procedure), which in turn are parallelized in streamwise direction.

The code has been optimized and run on the NEC SX-4 supercomputer cluster of the hww GmbH, Stuttgart (NEC SX-4/32 & NEC SX-4A/4, 8 GB RAM each). For the fine-resolution simulation described further down in Sect. 3.3 a uniform equidistant grid containing 2,754 × 193 × 89 (K = 44) points in (x,y,z)-directions (NX, NY, $2K+1$) has been employed needing 4 GB main memory, and 1 GB XMU memory. The computation of 3,600 time steps on the NEC SX-4/32 took 321,950 s, i.e., 3.7 μs per grid point, Fourier mode, and time step in the average. According to the built-in job statistics of the SX-4 the vector operation ratio was 98.7% with an average vector length of 183 points. Using 15 concurrent CPUs, the parallelized and vectorized code ran at 14,287 concurrent MFLOPS, and based on the total number of floating-point operations and the total execution time the job statistics indicated 1,063 MFLOPS per CPU. Compared to 2 GFLOPS theoretical peak performance per CPU this last number appears rather satisfactory. The performance, however, depends heavily on the load of the computer and the data just described were obtained on a day with a partly empty computer.

The y-discretization is the crucial point in resolution requirements for the present simulations. This is due to large-amplitude fluctuations impinging on the wall in the re-attachment zone. Therefore, in the high-resolution case, the

grid spacing was $\Delta x = 0.001875$, $\Delta y/\sqrt{Re} = 0.000982$ and $\Delta z = 0.004412$ ($\gamma_0 = 16$, $K = 44$).

3 Numerical Results

The present simulations are closely related to experiments in the so-called Laminar Wind Tunnel of the institute, where a LSB on a wing section with a chord-length of $\hat{c} = 0.615\,m$ was investigated (Würz *et al.* [9]). For this case the chord Reynolds number is $Re_c = 1.2 * 10^6$ and the free-stream velocity $\hat{U}_\infty = 29.3\frac{m}{s}$. For the computations the reference length $\hat{L}$ is chosen to be $6.15\,cm$, i.e., $1/10\,\hat{c}$. Hence, the Reynolds number for the simulation is 120,000 and $c = \hat{c}/\hat{L} = 10$. The computational grid, memory requirements and computation times have been already discussed in the previous section. At the disturbance strip a 2D disturbance, a so-called Tollmien–Schlichting (TS) wave, with non-dimensional frequency $\beta = 10$ and wall-normal amplitude $v/\sqrt{Re} = 10^{-6}$ is periodically forced. One wave length of the TS wave is discretized with approximately 160 grid points in x-direction and the time-wise resolution is 600 time steps per wave cycle.

3.1 Mean Flow

Averaging the resulting flow field over one or more disturbance cycles yields the time-averaged or mean flow. Streamlines and iso-vorticity contours of the averaged flow field are shown in Fig. 4. Note that the y-axis is enlarged by a factor of 10 with respect to x so that the actual separation bubble is shallower than it appears here. According to the streamlines the flow separates at $x \approx 7.1$ and re-attaches at $x \approx 8.15$. From separation to $x \approx 7.8$ there is a large dead-air region with only minor recirculating velocity which ends in a vortex centered around $x \approx 8.05$. The vorticity nicely portrays the separation of the boundary layer from the wall forming a quasi-free shear layer which somehow disintegrates at $x \approx 8.0$. Apart from this mean-flow effect the Tollmien–Schlichting wave and any other fluctuations are absent from the mean-flow data, of course. After re-attachment the wall vorticity and hence skin friction becomes very large.

Direct quantitative comparisons of these results with the experiments are presented in Figs. 5 and 6. The mean-flow profiles show a very good agreement with the experimental measurements, except for the last two stations close to the wall. Initially, the flow is attached from station A to B. The shear layer then lifts from the wall (C – E) and the profiles exhibit an inflection point away from the wall. If, as in the present experiments, a single hot wire is applied, it cannot be detected whether reverse flow is present. Moreover, introducing a probe into the bubble disturbs the flow, and the accuracy of the measurements deteriorates when large-amplitude fluctuations around a small mean amplitude occur. All this is true for the experimental data at stations E, F, and G.

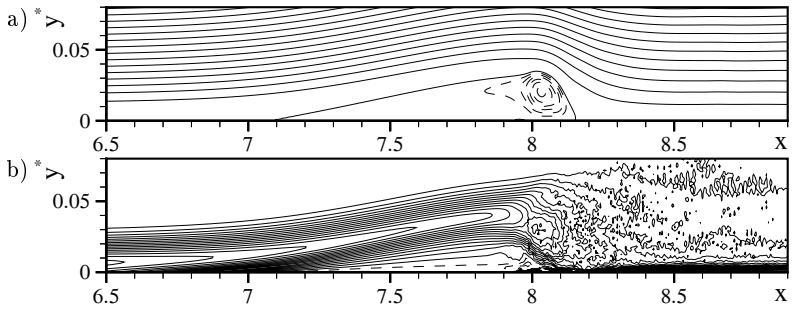

Fig. 4. Streamlines (a) and vorticity (b) of the mean flow; $y^* = y/\sqrt{Re}$.

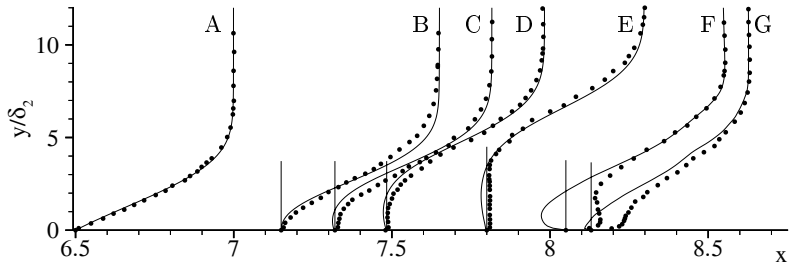

Fig. 5. Comparison of mean-flow profiles at different streamwise stations with the experiment. Symbols = experiment and lines = DNS. A – G = stations $x = 6.5$, 7.15, 7.32, 7.48, 7.8, 8.05, and 8.15, respectively.

Comparing the boundary-layer edge velocity u_e in Fig. 6 with the experiment shows the benefits of using the viscous-inviscid interaction model described in Maucher *et al.* [5]. The experimental data (circles) have been prescribed as potential edge velocity u_p in (3) and the simulation results yield an edge velocity u_e which is in very close agreement with the experiment (crosses).

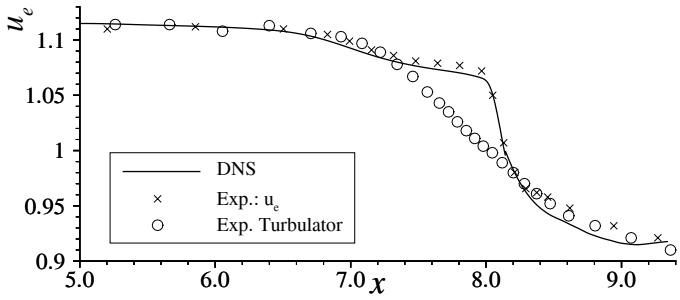

Fig. 6. Comparison of the boundary-layer edge velocity with the experimental results.

Actually, a rapid disintegration of the shear layer occurs starting between station E and F in Fig. 5, as already mentioned above. This is demonstrated by two visualizations of the instantaneous vorticity in the re-attachment region in Fig. 7. The momentary flow is strongly different from the averaged flow in Fig. 4 (note the absence of the strong recirculation vortex in the instantaneous data). Thus, the time-averaged data yield a completely wrong picture of the re-attachment zone. They have been used here only for comparison of the numerical results with the experiment because in most experimental realizations of the problem so far, only mean flow and statistical *rms*-data have been obtained. Since these data do not describe the actual flow physics in an adequate manner it is impossible to understand the underlying mechanisms and it appears plausible that an accurate modeling of the flow based on 2D time-averaged data or equations is at least critical.

3.2 Secondary Temporal Amplification

At sufficiently high Reynolds numbers 3D-disturbances are temporally amplified in the re-attachment region of the LSB once they are present due to interactions with a forced 2D wave. Similar to the mechanisms of secondary instability theory according to Herbert [1], Maucher *et al.* [4] found 3D amplification with subharmonic and fundamental frequency with respect to the forced 2D-wave for different spanwise wave numbers. In recent investigations the secondary temporal growth of 3D-modes in a large range of spanwise wave

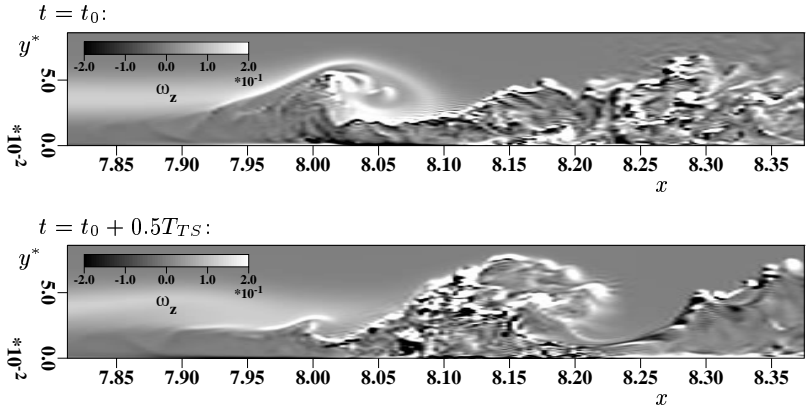

Fig. 7. Spanwise vorticity ω_z along the centerline ($z = 0$) in the vicinity of reattachment at two time-instances separated by one half forcing period T_{TS}; $y^* = y/\sqrt{Re}$.

numbers was investigated. Short pulse-like 3D excitations with very low amplitude and fixed spanwise wave number γ have been used to probe the 3D instability in DNS with a periodically forced 2D TS wave with an amplitude $A_{wall} = 10^{-5}$, i.e., 10 times larger than in the reference case. However, this did not enforce secondary instability by itself. Rather in the contrary: large 2D disturbances produce smaller and hence more stable LSBs.

For low γ there is no temporal secondary instability but up to very high values of γ 3D modes grow exponentially with the temporal growth rate $\beta_i = \frac{\partial}{\partial t}[\ln A(t_0 + t) - \ln A(t_0)]$. Figure 8 shows the temporal amplification rates β_i obtained from these DNS. The open and the filled symbols denote amplification of disturbances with subharmonic respectively fundamental frequency relative to the forcing.

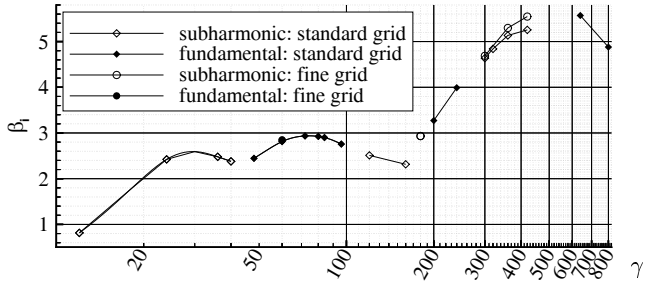

Fig. 8. Secondary temporal amplification rate β_i versus spanwise wave number $\gamma = 2\pi/\lambda_z$ for different discretizations.

Temporal secondary disturbance amplification starts around $\gamma \approx 10$ which corresponds to a ratio of wave numbers $\gamma/\alpha_{TS} \approx 0.5$, where $\alpha_{TS} = 2\pi/\lambda_{TS}$ ($\lambda_{TS} \approx 0.3$) is the streamwise wave number of the TS wave. For low spanwise wave number γ the subharmonic mechanism is observed. If γ is increased above $\gamma \approx 42$ the fundamental mechanism dominates. At $\gamma \approx 160$ a strong increase of the amplification rate sets in and either the fundamental or the subharmonic mechanism continues to dominate in an alternating manner. For validation, additional computations with a refined grid were performed (240 grid points per TS wave length, circles). Grid influence appears only for large $\gamma > 300$.

As already mentioned, the examination and interpretation of the time-averaged data in the rear-ward part of the LSB is highly misleading and unable to describe the flow physics since a phase with strong reverse flow alternates with a phase of positive u-velocity during each TS cycle. It turned out, that the phase with reverse flow is decisive for the secondary temporal amplification. The instantaneous vorticity field shows the roll-up of the 2D free shear layer in the re-attachment region (emphasized by contours of high vorticity in Fig. 9a). Apparently the shear layer is unstable with respect to 3D perturbations in the regions indicated by boxes, because 3D u' maxima occur at these positions, as is shown in Fig. 9b). The 3D disturbance maxima remain almost at a constant place during approximately one half of each TS period T_{TS}, i.e., as long as reverse 2D flow is present in the re-attachment region and their amplitude grows with respect to time during this phase. In the second phase the 2D velocity becomes positive and the uppermost part of the 3D perturbations is convected downstream together with the shear layer they are riding on (right column in Fig. 9). Thus, the onset of three-dimensionality happens inside the separation bubble where 3D perturbed fluid remains present from the previous TS period and where instantaneous high-shear layers are strongly unstable with respect to temporally growing 3D modes. In addition, it is highly conceivable that this re-entrainment of disturbances from the previous cycle contributes to the continuous temporal amplification of 3D modes. Finally, the amplitudes of secondary 3D modes saturate and an equilibrium state between 2D and 3D modes ends the transient phase. This state is discussed in the following subsection again for the fine-resolution simulation of the previous section.

3.3 Transition in the Reattachment Zone

When the 3D disturbances have saturated at large amplitudes the temporal growth ends and complex interactions between the 2D wave and the secondary 3D modes take place. The re-attachment region develops towards turbulence and the 2D wave is also affected compared to the transient case. Finally, the 2D wave attains its amplitude maximum in the re-attachment zone around $x \approx 8.0$ (Fig. 10 - thick solid line and triangles). From then on it decays towards the level of the 3D disturbances. Note the very good

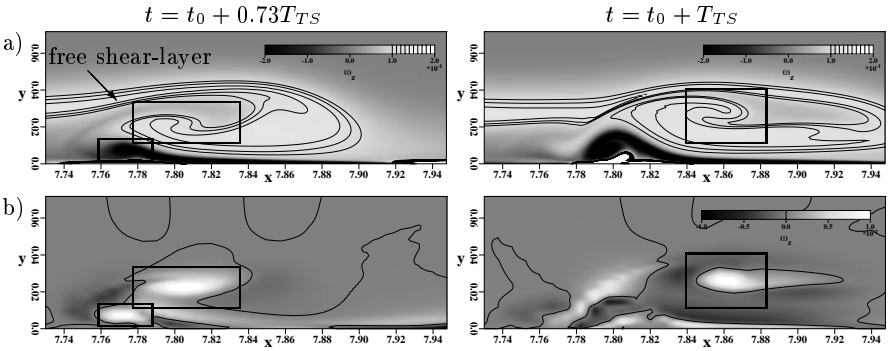

Fig. 9. Comparison of instantaneous 2D vorticity (a) with instantaneous 3D u'-distribution for $\gamma = 160$ (b) in the re-attachment zone; T_{TS} = fundamental 2D forcing period.

agreement of the amplification rate of the fundamental disturbance wave with linear stability theory (LST). However, this is not the case for the 2D higher harmonic (2, 0) because of nonlinear effects. The occurrence of many modes in the frequency/spanwise-wave-number spectrum means a disintegration of the flow structures (cf. Fig. 7). Apart from the dominance of the 2D disturbance such a picture is typical for laminar-turbulent transition.

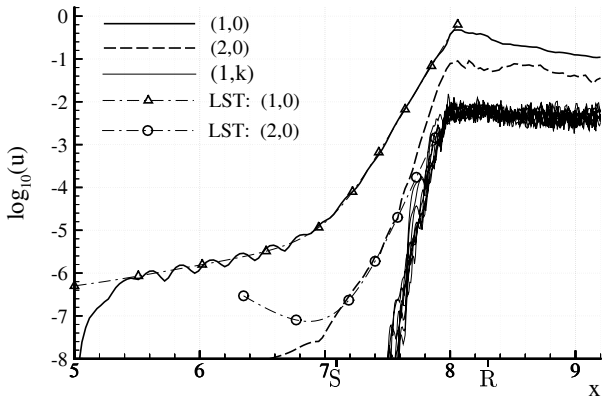

Fig. 10. Amplitude of the forced 2D wave (1,0), its first higher harmonic (2,0), and self-sustaining 3D modes (1,k), $\gamma = k\gamma_0$. Symbols indicate results of LST.

The breakdown of the free shear layer is visualized by iso-surfaces of the spanwise vorticity at four time instances during one TS cycle in Fig. 11. The x-domain shown begins well inside the separation zone and the iso-surface

$\omega_z = 0.1$ encloses the free shear layer as well as the vorticity maxima of the ensuing structures. At $t = T_0$ (a) the shear layer is almost 2D until $x = 8.05$. Afterwards, it is pierced by 3D perturbations from inside the reverse-flow zone and longitudinal vorticity structures build up at $x \approx 8.0$ ($t = T_0 + 0.25T_{TS}$, b) in the shear layer. Spanwise oriented 'rolls' which consist of fine-scale 3D structures leave the separation bubble (c+d) and comparatively calm phases appear in-between these rolls. Both phases are connected to the observations in subsection 3.2, each roll is a remainder of the roll-up of the 2D free shear layer and the calm phase occurs during the build-up phase of a new roll with new 3D disturbances. Because of their quasi 2D character despite their composition of very fine-scaled 3D flow structures the signature of these rolls in the frequency/spanwise-wave-number spectrum in Fig. 10 is a large amplitude 2D mode for $x > 8$. Finally it takes a remarkably long way downstream, until fully developed turbulence occurs and the dominance of the 2D wave (respective of the turbulent rolls) vanishes and an equilibrium turbulent boundary layer is reached.

The breakdown of the shear layer is further illustrated in cross-stream (y, z) cuts of the vorticity field ω_z in Fig. 12. Here the cutting plane is moving downstream with the evolving shear layer according to Fig. 11. The 2D free shear layer is centered around $y/\sqrt{Re} \approx 0.05$ and initially well above the 3D structures (a). But as the 3D disturbances get pushed up (b) the shear layer disintegrates and widens in wall-normal direction (c – d). The resulting structures are highly complicated and perhaps not yet grid independent for the present resolution. This must be investigated in further simulations.

4 Conclusions

The Navier–Stokes equations have been solved using a fourth-order accurate combined finite-difference spectral method to investigate laminar-turbulent transition in a laminar boundary layer that separates from the wall and re-attaches under the influence of turbulence, thus forming a so-called Laminar Separation Bubble (LSB). Without a well-adapted numerical scheme that exhibits good supercomputer performance through vectorization and parallelization, it would have been impractical to perform such simulations because of the large memory and computer time requirements caused by the small spatial and temporal step sizes needed for resolving the fine-scale unsteady fluid motions in the re-attachment zone of the bubble. Specifically, the code was run at 14 GFLOPS with 50% of the theoretical peak performance per node of the NEC SX/4-32 for regular computations.

The temporal mean flow of the present results agrees extremely well with experimental measurements performed in the laminar-flow wind tunnel of the institute but it is unable to describe the underlying flow physics. For the first time, a temporally growing secondary instability has been observed that amplifies 3D disturbances under the action of a 2D large-amplitude TS wave.

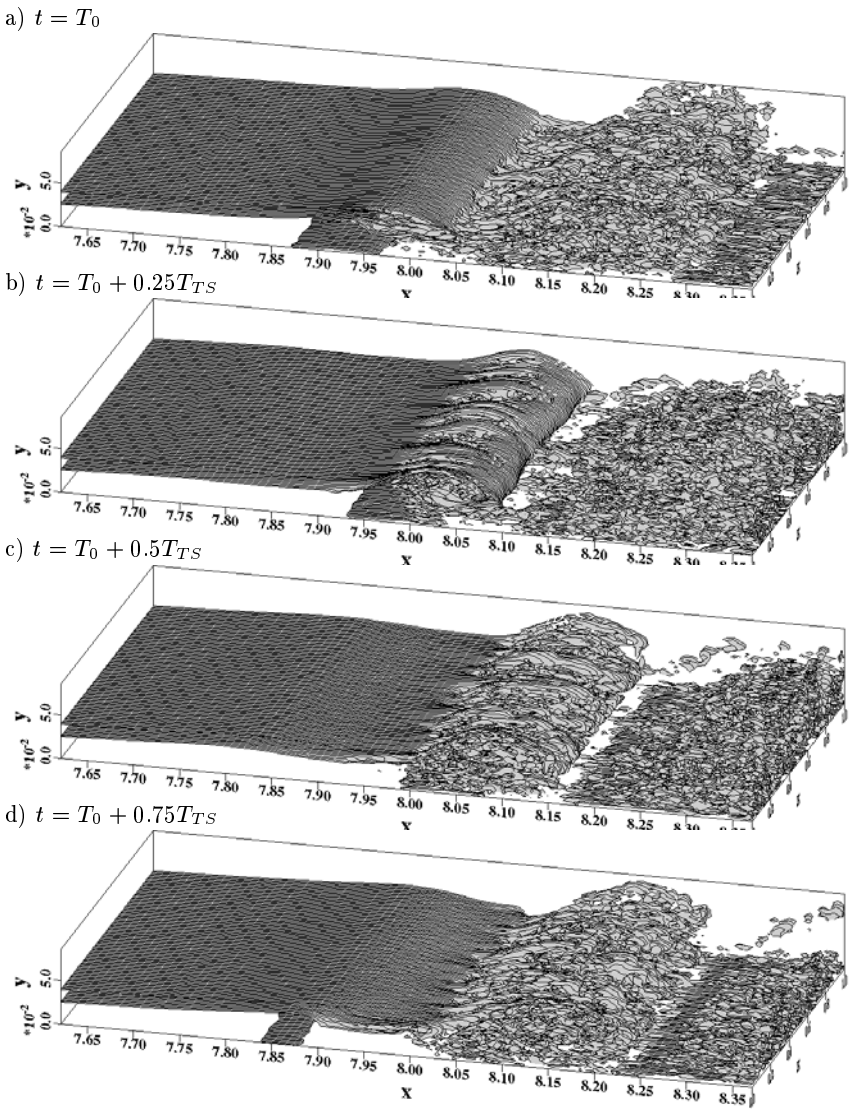

Fig. 11. Breakdown of the free shear layer into rolls of fine-scale turbulence. Isosurfaces of the spanwise vorticity at four instances of the TS-cycle T_{TS}.

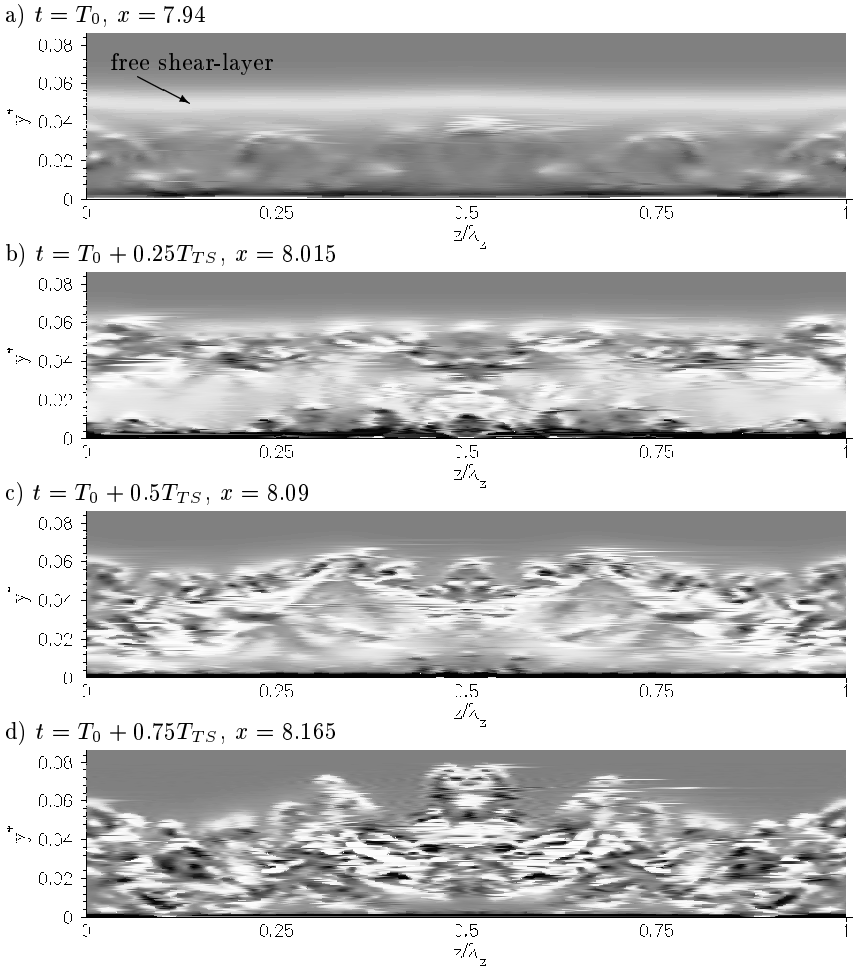

Fig. 12. Cross-stream cuts of the spanwise vorticity ω_z to illustrate the breakdown of the free shear layer.

The physical mechanism that leads to this instability has been identified as well: the entrainment of 3D disturbances by the roll-up of the 2D shear layer. Finally, high-resolution simulations have revealed the breakdown of the separated shear layer in the re-attachment zone. Again, 3D disturbances are entrained by the shear layer. They are carried away from the wall and pierce the undisturbed layer from underneath. This leads to an extremely rapid breakdown of the laminar flow into small-scale turbulence. However, the 2D disturbance remains visible for a certain distance downstream of the LSB, either in the frequency spectrum or as coherent structures in the ensuing boundary layer flow.

Acknowledgments

The financial support of this research by the Deutsche Forschungsgemeinschaft DFG under grant Ri 680/1 and by the Universität Stuttgart is gratefully acknowledged, as well as the provision of computer time by HLRS within the project LAMTUR.

References

1. T. Herbert. Secondary instability of boundary layers. In *Ann. Rev. of Fluid Mech.* **20** (1988) 487–526.
2. M. Kloker. A robust high-resolution split-type compact FD scheme for spatial direct numerical simulation of boundary-layer transition. *Appl. Scientif. Res.* **59** (1998) 353–377.
3. M. Kloker, U. Konzelmann, and H. Fasel. Outflow boundary conditions for spatial Navier-Stokes simulations of transitional boundary layers. *AIAA J.* **31** (1993) 620–628.
4. U. Maucher, U. Rist, and S. Wagner. Secondary instabilities in a laminar separation bubble. In H. Körner and R. Hilbig (Eds.) *New Results in Numerical and Experimental Fluid Mechanics*, Vieweg *NNFM* **60** (1997) 229–236.
5. U. Maucher, U. Rist, and S. Wagner. A refined method for DNS of transition in interacting boundary layers. AIAA 98-2435 (1998).
6. U. Rist. Nonlinear effects of 2D and 3D disturbances on laminar separation bubbles. In S.P. Lin (Ed.) *Proc. IUTAM-Symposium on Nonlinear Instability of Nonparallel flows*, Springer, New York (1994) 324–333.
7. U. Rist, U. Maucher, and S. Wagner. Direct numerical simulation of some fundamental problems related to transition in laminar separation bubbles. In Désidéri *et. al.* (Eds.), *Computational Methods in Applied Sciences '96*, John Wiley & Sons Ltd (1996) 319–325.
8. C. Stemmer, M. Kloker, U. Rist, and S. Wagner. DNS of point-source induced transition in an airfoil boundary-layer flow. In E. Krause and W. Jäger (Eds.), *High Performance Computing in Science and Engineering '98*, Springer, Berlin, Heidelberg (1998) 213–222.
9. W. Würz and S. Wagner. Experimental investigations of transition development in attached boundary layers and laminar separation bubbles. In H. Körner and

R. Hilbig (Eds.) *New Results in Numerical and Experimental Fluid Mechanics*, Vieweg *NNFM* **60** (1997) 413–420.